Single-cell analysis of osmoregulation reveals heterogeneity of aquaporin 4 functionality in human astrocytes

Peer-reviewed author version

Steenberghen, H; De Beuckeleer, S; HELLINGS, Niels; SOMERS, Veerle; Van Breedam, E; Ponsaerts , P; Nuydens, R; Maurin, H; Larsen, PH & De Vos, WH
(2024) Single-cell analysis of osmoregulation reveals heterogeneity of aquaporin 4 functionality in human astrocytes. In: Cytometry. Part A, 105 (12) , p. 870 -882.

DOI: 10.1002/cyto.a.24905
Handle: http://hdl.handle.net/1942/46270

Single-cell analysis of osmoregulation reveals heterogeneity of aquaporin 4 functionality in human astrocytes

Hugo Steenberghen[1,2], Sarah De Beuckeleer[1], Niels Hellings[3], Veerle Somers[3], Elise Van Breedam[4], Peter Ponsaerts[4], Rony Nuydens[1], Hervé Maurin[4], Peter H. Larsen[5,6], Winnok H. De Vos[1,7,8]

Affiliations

1) Lab of Cell Biology and Histology, Dept. Veterinary Sciences, University of Antwerp, Antwerpen, Belgium

2) Current affiliation: Biolizard NV, Foreestelaan 88, 9000 Ghent, Belgium

3) Department of Immunology and Infection, Biomedical Research Institute, Hasselt University, Diepenbeek, Belgium

4) Laboratory of Experimental Hematology, Vaccine and Infectious Disease Institute (Vaxinfectio), University of Antwerp, Antwerpen, Belgium

5) Janssen Research & Development, Division of Janssen Pharmaceutica N.V., Neuroscience Therapeutic Area, Turnhoutseweg 30, 2340 Beerse, Belgium

6) Current affiliation: Translational Research, Novo Nordisk, Novo Nordisk Park 1, 2760 Måløv, Denmark.

7) Antwerp Centre for Advanced Microscopy, University of Antwerp

8) µNEURO Centre of Research Excellence, University of Antwerp

Correspondence

Winnok H. De Vos, Lab of Cell Biology and Histology, Dept. Veterinary Sciences, University of Antwerp, Antwerpen, Belgium. Winnok.devos@uantwerpen.be

Abstract

Mounting evidence suggests that the water channel aquaporin 4 (AQP4) contributes to water flow and waste removal across the blood-brain barrier and that its levels, organization and localization are perturbed in various neurological diseases, including Alzheimer's Disease. This renders AQP4 a potentially valuable therapeutic target. However, most functional assays aimed at identifying modulators of AQP4 function are performed in primary rodent cells and do not consider inter-cellular variations in AQP4 abundance. To address this, we have established and applied a robust live cell microscopy assay that captures the contribution of AQP4 in the osmotically driven (de-)quenching of the vital dye Calcein-AM with single-cell resolution. Using human astrocytoma cells, we found that limiting the measurement to cellular regions instead of whole fields of view yielded a more sensitive readout of the osmotic response which correlated with total AQP4 abundance on the single-cell level. Stable co-expression of the two major AQP4 isoforms but not of the individual isoforms provoked a faster adaptation to osmotic changes. siRNA-mediated knockdown of *AQP4* had the opposite effect. Post-hoc correlation with the canonical membrane marker CD44 revealed that the speed of the osmotic response scaled with AQP4 membrane enrichment. Coating the substrate with laminin promoted a limited AQP4 membrane enrichment in the astrocytoma cells, while cell confinement with fixed-size micropatterns further increased the speed of osmo-regulation, underscoring the influence of extracellular factors. The osmotic response of primary fetal astrocytes and human iPSC-derived astrocyte models was comparable to AQP4-deficient astrocytoma cells, in line with their lower AQP4 levels and indicative of their immature state. In conclusion, a correlative single-cell approach based on the quantification of Calcein-AM quenching capacity, AQP4 abundance and AQP4 membrane enrichment, allows resolving osmoregulation in a more sensitive manner and reveals heterogeneity between and within human astrocyte cultures, which could prove crucial for future screens aimed at identifying AQP4 modulators.

Introduction

Aquaporin 4 (AQP4) is a protein that forms water channels at the end feet of astrocytes and which plays a central role in water homeostasis in the brain. It is composed of four subunits, each with six membrane-spanning alpha-helices forming a tetramer with a central pore. The pore facilitates transport of water across the cell membrane in response to osmotic changes[1]. The cytoplasmic and extracellular loops of AQP4 contain essential structural and functional domains that regulate the activity and expression of the protein. So far, 8 sense isoforms have been described, with the longer M1 and shorter M23 being the main 2 isoforms that have been observed in varying ratios in the brains of mammals[2]. AQP4 channels typically assemble into high density clusters called orthogonal arrays of particles (OAP) that amplify the water conductivity at the cell membrane. OAP dynamics are influenced by many factors, among which the level of AQP4 abundance, the ratio of its isoforms and the presence of anchoring proteins at the intra- or extracellular face of the membrane[3–5]. Disruption of proper AQP4 levels, polarization and OAP clustering have been implicated in various neurological diseases such as traumatic brain injury and stroke, *Neuromyelitis Optica* and Alzheimer's Disease (AD)[6,7]. For example, in AD patient brain samples and the Tg-AcrSwe mouse model of AD, an increase in overall AQP4 immunoreactivity was found along with a change in the ratio of M1/M23 isoforms and reduced presentation of AQP4 channels at the end feet of astrocytes[8,9]. This correlates with clinical symptoms such as the disturbance of sleep and the reduced waste removal through the glymphatic system in AD patients[10–12]. Therefore, understanding the role of AQP4 in this disease could help developing new therapeutic approaches[13].

AQP4 water channel functionality has been studied extensively using the osmotically driven (de-)quenching of the vital dye calcein-AM applied to oocytes, kidney cells, fibroblasts, primary cultures of rodent astrocytes [14–20]. Quantification of water conductivity in these non-human models has led to the discovery of novel minor AQP4 isoforms and potential AQP4 modulators such as TGN-20[19,21–23]. However, given the morphological, transcriptional and

proteomic differences of human astrocytes with their rodent counterparts, the translational value of this pioneering work could still be supported more by the use of human astrocyte models[24–27]. Human cell lines, such as HEK293, MCF7 breast cancer and a limited number of human astrocyte(-like) models such as U87MG, astrocytoma and SC1800 fetal primary human astrocytes have been described with osmotic perturbation assays. However, these are often performed at a cell population level, e.g., using a plate reader, disregarding the heterogeneity that is often present within cell cultures[28–31]. As such, these assays may be biased by growth differences or the presence of subpopulations, and they do not allow relating osmoregulation to the molecular markup of individual cells. To address this, we adapted the classical osmotic assay to a microscopy format that allows single cell measurements and combined it with post-hoc immunostaining for proteomic profiling of the same cells. Using this assay, we evaluated osmoregulation in different primary, immortalized and human iPSC-derived astrocyte models. We found inter and intra-cellular differences, which could be linked to AQP4 abundance and membrane enrichment and found that changing the composition and geometry of the substrate influenced osmotic tuning speed.

Materials and methods

Patient serum samples

Anonymized serum samples of *Neuromyelitis Optica* (NMO) patients were obtained at the University Biobank Limburg (UBiLim). This study was approved by the ethics board of the University of Antwerp/UZA (Project ID 5323). Commercial human control serum was used as a control (Sigma-Aldrich H4522-100ML).

Stable cell line generation

1321N1 derived astrocytoma cell lines were generated and provided by dr. Stefan Masure (Janssen Pharmaceutica N.V., Beerse, Belgium). Three different transfected clones were generated from the wildtype 1321N1 astrocytoma control line (WT; ECACC 86030402): hAQP4-M23~pcDNA3.1hygro (M23), transfected using Fugene6 (Roche E2691) and maintained with 100µg/ml Hygromycin B (Sigma, 400052), hAQP4-M1~pcDNA3.1G418 (M1), transfected using Lipofectamine2000 (Invitrogen, 11668019) and maintained with 400µg/ml G418 (Sigma, 345810) and finally a clone containing both constructs (M1M23) was generated and maintained with 400µg/ml G418 and 100µg/ml Hygromycin B.

To generate individual clones, cells were seeded in 15 petri-dishes of 50 cm2 (mother plates) at a density of 10000 cells/cm² in specific growth medium, Dulbecco's modified Eagle's medium (Gibco, UK) enriched with 10 v% heat inactivated fetal calf serum (Hyclone, US), 2 mM glutamine (Sigma; US), 1 mM pyruvate (Boehringer, Germany), 100000 IU/l Penicillin G (Serva, Germany) and 100 µg/ml Streptomycin (Serva, Germany). The cells were incubated overnight at 37°C in 5% CO2 and subcloning was performed by limiting dilution. When a clone was isolated, it was cultivated in a 75 cm² culture flask. Finally, monoclonals were obtained, which were tested for AQP4 expression level and intracellular distribution. As control, non-transfected cells (WT astrocytoma cells) were used.

Cell culture

After generation, all 1321N1 lines were maintained in Dulbecco's modified Eagle's medium (Gibco, 41966029) supplemented with 10 v% heat-inactivated fetal bovine serum (FBS; Life Technologies, 10500064) at 37°C and 5% CO2. Cultures were split 1:6-1:12 twice a week when reaching 90% confluence using trypsin-EDTA (Gibco, 25200072). AQP4 cDNA-transfected cells were maintained in medium supplemented with their respective antibiotics.

For the comparison of different cell substrates and micro-patterned well plates, 96-well plates (Greiner Bio-One 655096) were first coated for 4 hours with 50µl 0.1 mg/ml poly-L-ornithine (PLO; Sigma, A-004-M), then washed 3 times with PBS and finally incubated 1 hour with mouse laminin at 10µg/ml (PLO-mLAM; Sigma L2020) before cell seeding. Micropatterned plates (CYTOO, 20-012-00) were coated with 50µl 10µg/ml laminin for 1 hour before seeding cells at 12500 cells/cm^2.

For the comparison with the astrocytoma cells, passage 7-9 primary astrocytes (Sciencell #1800, hence further referred to as SC1800) were cultured according to the manufacturer's guidelines in the proprietary astrocyte medium included in the kit (Sciencell #1801) on plastic bottom 25 cm^2 culture flasks without the addition of antibiotics. These astrocytes were dissociated with accutase (Invitrogen, 00-4555-56) and seeded at 15625 cells/cm^2 in supplemented SC1801 medium on uncoated 96-well imaging plates alongside wells with WT and M1M23 cells at densities of 12500 cells/cm^2 and 15625 cells/cm^2 respectively.

Differentiation of neural precursor cells

Neural precursor cells (NSC) where differentiated into astrocyte precursor cells (APC), as previously described [32,33]. In brief, NSC were thawed and centrifugated at 250 rcf without delay to remove DMSO. They were then seeded on 1X Matrigel-coated (Corning, 354277) 6-well plates and maintained for 7 days with fresh 1:1 Neurobasal Medium (Gibco, 21103049):Advanced DMEM:F12, (Gibco, 12634010) supplemented with 1X Neural Induction supplement (A1647801, Gibco) and 1% penicillin–streptomycin (Gibco, 15070063)

every 48 hours. After 7 days, NSC were split and seeded at 15000 cells/cm^2 and changed to SC1801 medium without antibiotics after 48 hours. Medium changes were performed twice weekly initially and weekly after 7 days until the experiments. SOX9 transcription factor inducible astrocytes (iSOX) were generated from recombinant iPSC generously provided by Prof. dr. Catherine Verfaillie[34]. The recombinant normal donor iPSC clone contained a doxycycline-inducible TETO-ON system for overexpression of SOX9 (SOX9-iPSC). SOX9-iPSCs were seeded at 150,000 cells/cm² on Matrigel-coated plates in mTeSR1 with Revitacell (Gibco, A2644501). After one day, cells were cultured in NI medium for 12 days, with daily media changes. Subsequently, cells were plated at 65,000 cells/cm² on Matrigel-coated plates in NMM with bFGF (PeproTech, 100-18C) and Revitacell, followed by maturation medium the next day. Maturation medium, a 1:1 Neurobasal/DMEM-F12 mixture supplemented with N2, sodium pyruvate (Gibco, 11360039), Glutamax, N-acetyl-cysteine (Sigma, A7250), db-cAMP (Sigma, D0627), CNTF (PeproTech, 450-13), BMP4 (PeproTech, 120-05ET), and HB-EGF (PeproTech, 100-47), was used with doxycycline (Sigma, D9891) for the first 6 days (replaced every other day) and without doxycycline thereafter (changed twice weekly). Upon reaching >90% confluency, cells were replated at 20,000 cells/cm² in maturation medium and kept 27 days with medium changes twice weekly until the experiments.

siRNA mediated knockdown of AQP4 in M1M23

WT and M1M23 at passage 14-18 were seeded at 12500 cells/cm^2 and 15625 cells/cm^2 respectively in 12-well plates. After 24 hours cells were transfected with a medium only sham treatment (Sham), 25µM non-targeting siRNA control (NTC) or 25µM AQP4 siRNA (AQP4-KD; TriFECTa, Integrated DNA Technologies, 231954627 sequence_id:hs.Ri.AQP4.13.3) in DMEM without supplementation at room temperature for 25 minutes according to the transfection kit manufacturer's instructions (Mirus Bio Trans-it TKO MIR 2154) and incubated at 37°C and 5% CO_2 for 24 hours in culture medium.

RNA extraction, cDNA conversion and RT-qPCR

RNA extraction was performed according to the manufacturer's instructions (Qiagen RNeasy Mini, 74104) and samples transferred to dry ice immediately after treatment with lysis buffer. RNA was diluted in RNase-free water to a final volume of 30µl and stored at -80°C in 5 µl aliquots. Quality control and concentration measurement was done using Agilent RNA 6000 Nano kit according to the manufacturer's instructions (Agilent technologies 5067-1511). Only samples with RIN above 8 were used and RNA was diluted for each sample to match the concentration before cDNA conversion with the iScript cDNA synthesis kit (Bio-rad, 1708891). RT-qPCR master mix was prepared with SsoAdvanced Universal SYBR Green Supermix (Bio-rad, 1725272). A single qPCR reaction required 5µl SYBR-green Supermix, 2µl molecular grade H2O and 0,5µl 10µM forward and reverse primer solution corresponding to the desired target sequences (Fig. S2B). All primers were validated by inspection of the melting curve and calculation of the primer efficiency from a dilution series (efficiency range = [1.8-2.2]; data not shown). RT-qPCR reactions were always run in duplicate and no-template and no-reverse transcription controls were included in each run (max. 35 cycles).

Osmotic assay

Live cell Calcein-AM self-quenching assays have been previously reported[14,35]. In brief, WT, M1, M23 and/or M1M23 cells (passage number 12-20) were detached with trypsin and seeded in a plastic bottom black 96-well plate (Greiner, 655090 and Cellvis, P96-1.5P) 48 hours before start of the assay at a final density of or 15625 cells/cm^2 and 12500 cells/cm^2 respectively to account for differences in growth rate. For the comparison of WT, M1M23 and SC1800 (passage 8-10) no additional coating was added to the plates. For osmotic assays with SC1800 (passage 2-4), DIV47 APC and DIV27 iSOX, cells were detached with accutase and seeded at 37500 cells/cm^2 on PLO-mLAM plates 96-well plates. Cells were kept at 37°C and 5% CO_2. Before imaging, medium was removed, followed by a washing step with HBSS with Ca^{2+} and

Mg^{2+} (Gibco, 14025-092) supplemented with 14 mM HEPES (Sigma, H0887-100ML) (HH-buffer). Calcein-AM (Invitrogen, C3100MF) was dissolved in dimethyl sulfoxide (DMSO; Sigma, D2650) and diluted 1:100 to a final concentration 10 µM in HH-buffer, which was added to the cells for 45 minutes (37°C, 5% CO_2). Cells were then washed once more with HH-buffer and 100µl HH-buffer was added to the cells as the baseline volume for imaging. For the highest stimulation condition, only 50µl HH-buffer was added.

Calcein quenching kinetics were recorded per well according to a standard sequence of recording baseline fluorescence for 10 seconds at 300 mOsm/l (manufacturer's estimate), followed by a prompt administration of 50µl hyperosmotic solution (0, 0.1M, 0.2M, 0.3M, 0.4M NaCl in HH-buffer) raising the osmolality of the solution (to 300, 375, 450, 600 and 900 mOsm/l, respectively). After recording for 40 seconds, 150µl ultrapure distilled H_2O (ddH_2O) was added to the well, gradually lowering the osmolality in the well back to the baseline value of 300 mOsm/l. For the 0.4M NaCl stimulus, the starting volume was lowered to 50µl, 50µl hyperosmotic saline was injected and 200µl ddH_2O was added to return to isotonicity within the 300µl volume of the well. A minimum of 3 technical replicates (wells) was used per 96-well plate and at least 3 wells were not stimulated during imaging to allow post-hoc photobleaching correction. For each experiment, osmotic assays were performed on 3-4 separate days unless stated otherwise.

After treatment of all wells, half of the imaging buffer was removed and cells were fixed by adding 4 v% methanol-stabilized paraformaldehyde (PFA; Roth, 3105.2) for 20 minutes at a final PFA concentration of 2 v%. Afterwards, all wells were washed twice using in-house prepared 0.01M phosphate buffered saline (PBS; Gibco, 14190-094) and stored in in-house made 0.01M PBS with 0.1 v% sodium azide (Sigma, 71290) at 4°C.

To evaluate osmotic changes at the level of the nucleus, a similar approach was used with SiR-DNA, a far-red live cell fluorogenic DNA labelling probe (Spirochrome, SC007; 652nm/674nm). The dye was stored in DMSO at -20°C at a concentration of 1mM and diluted

1:1000 in HBSS for use with the WT, M1, M23 and M1M23 cells. Here, no photobleaching correction was performed.

Immunofluorescence

Cells were washed 10 minutes with PBS, followed by 3 minutes of permeabilization using PBS supplemented with 0.5 v% thimerosal (Fluka, 71230), 0.1 v% sodium azide, 0.3 v% bovine serum albumin (Sigma, A7284) a 10 v% normal horse serum (Merck, H1270) (PAV buffer) with 0.1 v% Triton X-100 (Sigma, X100). The cells were incubated overnight at 4°C in PAV buffer containing rabbit polyclonal antibodies specific to an intracellular C-terminal site of AQP4 (Sigma-Aldrich, HPA014784) diluted 1:100 and mouse monoclonal antibodies to CD44 (Sigma, MAB4065) at 1:200. A no primary antibody control was always included (NPC). Subsequently, samples were washed with PBS twice for 5 minutes. The cells were incubated with Cy3-labeled donkey anti-rabbit antibodies (Jackson Laboratories, 711-165-152) and Fluorescein (FITC)-labeled donkey anti-mouse antibodies (Jackson Laboratories, 715-095-151), all diluted at 1:1000 in PAV for 2 hours.

For the comparison of permeabilization agents PBS alone, 0.1% Triton-X100 (PBS-T) in PBS or 0.1% saponin (Sigma, S-4521) in PBS was used for 3 minutes before the primary antibody labeling, before continuing the staining protocol with PBS instead of PAV for the secondary antibody labeling.

For the immunocytochemistry using NMO sera, a dilution series was prepared of each serum sample (PS) and a healthy control (HS; Sigma-Aldrich, H4522-100ML) from 5-160x dilution in PAV buffer and incubated overnight at 4°C on the cells without prior permeabilization. Afterwards, the cells were gently washed once after which they were incubated with Alexa Fluor 488-labeled goat anti-human antibodies (Invitrogen, H10120) at 1:750 in PBS in the dark for 2 hours.

Finally, all cells were incubated with 5 µM/ml 4′,6-diamidino-2-phenylindole (DAPI; Sigma, D9542-10MG) and 2µg/ml CellMask (Invitrogen, H32721) for 30 minutes, followed by two 5-minute washes with PBS and storage in PBS with 0.1 v% sodium azide at 4°C before imaging within the week.

Microscopy

Live cell and corresponding immunostained images were acquired using a Nikon Ti2 epifluorescence microscope with automated stage and SpectraX LED light source (Lumencor). Per well, a point was chosen around the center and a single time series was recorded at 7.3 frames-per-second. Excitation and emission spectra were separated by a quad bs + m (395, 470, 555, 640nm) dichroic filter (Lumencor) and single band emission filters (DAPI: Ex. 395/25nm, Em. 435/26nm, Calcein-AM/FITC: Ex. 470/24nm, Em. 510/40nm, Cy3: Ex. 555/25nm, Em. 595/40nm, Cellmask: Ex. 640/30nm, Em. 705/72nm). A Nikon DS-Qi2 detector was used to capture the signal through a 10X (NA 0.3; Figure 1) or 20X (NA 0.75; Figure 2,3,5) air objective. For the individual immunostaining of AQP4, CD44 and NMO patient sera, a spinning-disk confocal microscope setup (Yokogawa CSU-W1) was used to capture 15 µm z-stacks with a step size of 1 µm or 1.5 µm (fixed within experiments) using a 20X (NA 0.75) or 40X (NA 0.95) air objective respectively (Nikon). Well mean values were calculated based on a random sampling of 16-25 images per well (after removal of empty images or images with artefacts).

Data analysis

Fiji is just ImageJ software[36] (Fiji, version 1.53t) was used to visualize, preprocess and extract image and cell intensity data as well as area measurements from Calcein-AM images using the Fluxometrics.ijm script available at Github/DeVosLab. For the comparison of imagen and cell-based calcein-AM readouts, the mean calcein-AM signal intensity was extracted with and

276 without segmentation of cells in the average projected image. No background correction was
277 applied to allow direct comparison of whole field and cell-based measurements. In short, for
278 threshold-based segmentation first a gaussian blur with diameter 1 was applied on the average
279 projected calcein-AM signal, followed by fixed thresholding and separation of individual cells
280 by watershed separation and finally feature extraction.
281 Further analyses were performed in R[37]. The mean fluorescence intensity was normalized to
282 the mean intensity of the first second and corrected for photobleaching by dividing the values
283 with the fitted average intensity per time point of the untreated wells per plate. In a variable
284 window around the inflection point[38], the rate of fluorescence change after hyperosmotic
285 stimulation (decay rate) and the addition of H_2O (recovery rate) was captured by fitting an
286 asymptotic regression model using nonlinear least squares parameter estimation (SSasymp
287 function)[37]. The time constant -e^{lrc} (decay rate and recovery rate) from the formula $output =$
288 $asym + (R_0 - asym) * e^{(-input * e^{lrc})}$ reflects the rate of fluorescence change and was used to
289 compare different conditions. Other parameters that changed under the influence of the osmotic
290 stimulus were the minimum and maximum of the intensity reached after the respective
291 stimulation and recovery injections. The percentage recovery (recovery) between the final
292 intensity and baseline intensity was also calculated, as well as the percentage overshoot of the
293 maximum fluorescence after the recovery injection (overshoot) compared to the value at the
294 end of the experiment.
295 Quantification of immunoreactivity for AQP4 and CD44 as well as morphological feature and
296 calcein quenching kinetics parameter extraction were done on the same regions to allow their
297 correlation at the single-cell level. To achieve this, the microscope stage positions of the initial
298 imaging were recorded in Nikon NIS-elements during calcein imaging and used to record
299 images on the same location after immunocytochemistry, with minimal manual correction
300 where needed. Pre- and post-immunocytochemistry images were then aligned in FIJI using an

301 in-house script using intensity maxima of the calcein-AM images and Cellmask images to
302 perform minimal XY-shifts as needed. Further image quantification was done with
303 Cellblocks.ijm macro suite, using StarDist and Cellpose for nuclear and cell segmentation
304 respectively (Github/DeVosLab)[39–41].
305 For separate quantification of AQP4 and/or CD44 immunoreactivity, maximum projected
306 confocal images were segmented with StarDist and Cellpose for nuclear and cell segmentation
307 respectively, followed by feature extraction with Cellblock.ijm. Pearson correlation within
308 previously segmented cell ROIs was measured using the BIOP implementation of the Imagej
309 plugin JaCoP[42]. Visualization, calculation of time constants and statistical analysis was
310 performed in R (version 2023.03.0 Build 386) using RStudio[37,43]. When not indicated
311 specifically, mean ± standard deviation is reported (SD).
312

Results

Cell-selective registration of Calcein-AM (de-)quenching increases sensitivity of osmotic response measurements.

The measurement of the osmotic response is based on the self-quenching properties of the cell-permeable, inert, fluorescent dye Calcein-AM. A hyperosmotic stimulus, via the addition of NaCl, triggers cell shrinkage and concomitant loss of fluorescence due to quenching, whereas a subsequent hypo-osmotic stimulus through the addition of ddH_2O has the opposite effect[35]. Previous studies have used a plate reader to obtain a fast readout of the osmotic response in a population of cells[14]. However, such an approach negates the underlying cellular heterogeneity and precludes a direct relation with the molecular composition of individual cells. To resolve this, we implemented an automated microscopy-based approach that still offers the necessary throughput for functional screening (Fig. 1A).

We first evaluated the stability of the calcein-AM dye within the experimental timeframe. The average baseline Calcein-AM intensity was stable over a period of 150 minutes (Fig. S1A) and had a mean intra-run coefficient of variance of 0.090. Variability between runs on separate days was low with a coefficient of variation of 0.061, illustrating robust and reproducible staining (Fig. S1B). Upon imaging without any interventions, the Calcein-AM intensity decreased by 18±7 % due to photobleaching within the 90 second time span (Fig. S1C). All raw intensity measurements were therefore normalized to the average photobleaching across the imaging plate (yielding a normalized calcein intensity, see M&M).

Using *AQP4 M1* and *M23*-overexpressing 1321N1 human astrocytoma cells (further referred to as M1M23 cells), we visually confirmed the effect of hyper and hypoosmotic stimulation on the threshold-based segmentations of cells was limited for these adherent cells, only causing unacceptable distortions of the segmented masks when applying harsh stimuli of over 750 mOsm/l which also induced overt blebbing and even loss of signal after H_2O administration, indicating cell damage and even cell rupture (Fig S1G). Using these observations as an

indication, we further sought to establish the maximal osmotic stimulation that was still reversible. To this end, we stimulated the cells with a range of hyperosmotic solutions, followed by an equivalent addition of ddH_2O to restore isotonicity (Fig. 1B, C). Using From the normalized intensity traces, we calculated a set of characteristic parameters describing the dynamic range of the signal (based on the minimum and maximum intensities of the traces), the decay rate after NaCl addition, and the recovery rate and overshoot after ddH_2O addition (Fig. 1D, S1D). The dynamic range and overshoot increased with increasing osmotic stimuli, but the maximal reversible effect was achieved for a hyperosmotic stimulus that raised the osmolarity to 600 mOsm/l (0.45M NaCl; Fig. 1E). Using this concentration, we next analyzed the variability of the main parameters as a function of time and the reproducibility across replicates. When inspecting the images obtained from whole well plate imaging between different runs, we noticed significant variability in cell density (Fig. 1F). This affected several metrics including baseline intensity, dynamic range, decay rate and overshoot when measured across the full field of view. When limiting the measurement to the cellular regions of interest, a more consistent response was measured. which was typified by a consistently larger dynamic range, less variable kinetics parameters and an overall increased robustness to differences in cell density. For example, in image-based analysis without additional background correction, the measurement of the overshoot becomes diluted by background signal (Fig. 1G, S1E). Thus, cell-based assessment of Calcein-AM (de-)quenching kinetics allows for optimal visual evaluation of cell treatments and enables a robust analysis, even when cell population density is heterogeneous across the imaging plates.

AQP4 abundance tunes osmotic response rate.

To validate the role of AQP4 in the response of astrocytoma cells to osmotic changes, we used the cell-based analysis to compare the M1M23 with their wild type counterparts (further referred to as WT cells), which display no detectable *AQP4* expression. To improve cell

segmentation on the single-cell level, we also adopted Cellpose in in the analysis workflow[39]. The M1M23 and WT cells showed comparable baseline and endpoint fluorescence levels as well as a similar dynamic range between relaxed and quenched states. However, the M1M23 showed a much faster response to both hyper- and hypo-osmotic stimuli, as reflected by their significantly smaller decay (1.02±0.47 in M1M23 *vs.* 1.71±0.34 in WT) and recovery rate (1.13±0.33 in M1M23 *vs.* 1.77±0.40 in WT) (Fig. 2 A, B). M1M23 cells also displayed an overshoot in response to the recovery ddH_2O injection. To confirm that the observed effects in M1M23 cells were truly driven by AQP4 overexpression as opposed to *e.g.,* clonal effects, we subjected these cells to an siRNA-mediated knockdown of *AQP4* (AQP4 KD), targeting a conserved coding sequence of both isoforms. Effective depletion of AQP4 was validated at the transcript level (89% decrease compared to NTC at 48h) and protein level (29% decrease compared to NTC at 72h) (Fig. 2C-E). At 72h after transfection, knockdown of *AQP4* caused a significant increase in the decay rate of M1M23 cells compared to NTC-treated M1M23 cells (1.57±0.77 *vs.* 0.84±0.53), while it had no significant effect on the decay rate of the AQP4 KD-treated WT cells compared to NTC-treated WT cells (1.97±0.32 *vs*. 1.97±0.423; Fig. 2F). This confirms that AQP4 affects the rate with which cells respond to osmotic changes.

To gain further insights into the correlation of the live cell readouts and AQP4 abundance of those cells, we used image registration to align the post-hoc immunocytochemistry images with the already generated live-cell calcein-AM images and used the addition a nuclear staining to further improve segmentation of individual cells (Fig. S1F).

When comparing the osmotic response using the decay rate as representative parameter to the AQP4 levels at the single-cell level, we retrieved a linear trend in line with the population level results. However, the linear relationship was not as strong as one would expect based on the former experiments (Pearson correlation coefficient = 0.43, R^2 = 0.18; Fig. 2G). Furthermore, there was significant heterogeneity in the osmotic response even between cells with higher AQP4 levels. This suggests that the total cellular abundance of AQP4 is not a sufficient

prerequisite for osmotic buffering, but rather its functional integration into the cell membrane. In line with this, overexpression of individual *AQP4-M1* and *AQP4-M23* isoforms (which are expected to form different arrays) had much less pronounced effect on the decay rate than the combined overexpression while significantly increasing recovery for M1M23 and M23 but not the M1 line. However this may also be due to the allover lower transcript levels, as measured by qPCR (Fig. 2H-K, S2A). We therefore conclude that the model cells show a heterogeneous but expected response when overexpressing AQP4 and its individual isoforms, yet the contribution of the ratio of both isoforms to functionally relevant phenomena such as OAP formation cannot be untangled within the current experimental setup[18,44,45].

Given the intricate mechanical and biochemical coupling between the cytoplasm and nucleus, we asked to what extent differences in osmoregulation between cells would translate into their nuclear remodeling. Therefore, we exploited the self-quenching property of SiR-DNA, a vital DNA-binding rhodamine analog[46,47], to perform similar intensity measurements of the nucleus of M1M23 cells during the osmotic assay. The intensity kinetics of SiR-DNA, were comparable to those of Calcein-AM (Fig. S2C, D), but the decay and recovery were slower, subtler and did not differ between the cell lines (Fig. S2E). We therefore conclude that the nucleus does not sense the osmotic tuning conferred by AQP4, at least not within the studied timeframe.

Human fetal astrocytes and iPSC-derived astrocytes do not show enhanced osmoregulation

Given the transformed nature of 1321N1 cells, a more faithful mortal human astrocyte model may be preferred from a translational perspective. Therefore, we evaluated the osmoregulation of a commercially available fetal primary astrocyte line SC1800, which is often used control line for astrocyte differentiation[32,34,48], as well as two iPSC-derived astrocyte models (iSOX and APC). iSOX cells contain an inducible SOX9 cassette to drive astrocyte differentiation, whereas the APC line induced towards astrocytes from an NPC stage using chemically defined medium[32–34]. All three cell types showed a similar yet slightly more pronounced branching

morphology to the 1321N1 cells (Fig. 3A). All three models responded to both the hyperosmotic and hypoosmotic stimuli (Fig. 3B). In an initial comparison with the astrocytoma cells, SC1800 (at passage 8-10) showed no distinct difference in decay and recovery rate from the WT astrocytoma cell line (3.00±0.53 *vs*. 2.92±0.38; Fig. 3C). In a separate comparison of the iSOX, APC and SC1800 cells (at passage 2-4) the APC cells showed a slower decay rate after hyperosmotic stimulus compared to the SC1800 (2.12±0.28 *vs.* 1.71±0.32) and iSOX astrocytes (1.62±0.43), while the recovery rate did not differ significantly between the three. The osmotic response rates did not scale with the AQP4 levels as measured by quantitative immunocytochemistry (Fig. 3D) and there was little correlation between the AQP4 intensity and decay rate at single cell level (Fig. 3E), suggesting these cells do not yet dispose of significant aquaporin functionality.

ECM modification affects M1M23 cell size and correlation between AQP4 membrane enrichment

Given the limited responses in the iPSC and primary astrocyte models, we next investigated whether the osmoregulation in M1M23 could be further enhanced and homogenized by tuning the substrate conditions. In rat primary astrocytes, AQP4 membrane presentation could be modified by changing the composition of the extracellular matrix[49,50]. We therefore tested the effect of coating the substrate with poly-L-ornithine (PLO) and laminin (PLO-mLAM). Cells plated on PLO-mLAM coated substrates showed a reduced and less variable cell size (742±75 μm^2 for WT *vs.* 926±178 μm^2 for M1M23 without coating, 733±81 μm^2 for WT *vs.* 793±183 μm^2 for M1M23 with PLO-mLAM). Although we measured no change in AQP4 levels with quantitative immunofluorescence (Fig. 4A-C) in cells grown on PLO-mLAM , the correlation with membrane receptor CD44 was increased (1.04±0.03 with *vs.* 0.93±0.07 without coating), suggesting an enhanced enrichment of AQP4 at the plasma membrane. As a first step towards single-cell quantification of membrane-presented AQP4 beyond total AQP4 quantification, we

443 investigated the use of sera from *Neuromyelitis Optica* (NMO) patients, which contain anti-
444 AQP4 antibodies that preferentially bind the M23 isoform of AQP4. Without additional
445 permeabilization with Triton X-100 or saponin the commercial anti-AQP4 antibody did not
446 show any signal, illustrative of its intracellular epitope specificity (Fig. S3A). In contrast, one
447 serum from an NMO patient still showed a significantly higher signal as compared to a control
448 serum without permeabilization, suggesting it has the potential to bind an extracellular epitope
449 (Fig S3B. However, the limited accessibility and lack of reactivity in two other patient sera,
450 precluded us from further using it to quantify AQP4 membrane presentation.
451
452 *Single-cell patterning improves osmotic readout.*
453 Despite the observed increase in membrane enrichment of AQP4 upon substrate
454 functionalization, cells still displayed heterogeneous AQP4 localization patterns. Furthermore,
455 *in vivo*, astrocytes display a polarized organization with increased AQP4 presentation at the
456 end feet. To obtain a more homogeneous and polarized phenotype, we used Y-shaped micro-
457 patterns with 1600 μm^2 surface area coated with laminin (Fig. 5A). Seeding cells onto these
458 micropatterns increased the mean AQP4 intensity in the cell body and at the cell border
459 compared to non-patterned cells on plastic bottom plates with PLO-mLAM coating (Fig. 5B).
460 Consistently, when applying the Calcein-AM quenching assay to micropatterned astrocytoma
461 cells using the osmotic stimulation assay 4 hours after seeding the cells, a much sharper
462 response could be observed in the Y-micropatterned M1M23 cells compared to cells seeded on
463 PLO-mLAM-coated plates without micropatterns (Fig. 5C). Given the rapid responses of
464 M1M23 cells seeded on Y-patterned plates leading to poor asymptotic fit, a slope calculation
465 was performed at the inflection point instead of calculating the time constant of the fitted
466 asymptotic model. Whereas both assays detected a difference in M1M23 versus the WT in both
467 simulation and recovery slopes, the WT cells did not differ significantly in their simulation
468 slope on the Y-micropatterns (-0.07±0.03 *vs.* -0.04±0.02). The M1M23 on the Y-micropatterns

469 on the other hand reacted significantly faster than their regular counterparts (-0.22±0.08 *vs.* -
470 0.15±0.06). Fitting a Michaelis-Menten kinetics model confirmed the non-linear relationship
471 of AQP4 intensity with the response rate of 1321N1 cells (Fig. 5D). Cells with high AQP4
472 abundance near the cell membrane also showed the strongest osmotic response saturating at
473 around 0.25 for the stimulation slope and 0.28 for the recovery slope. Thus, when confined by
474 micropatterns, the AQP4-driven osmoregulation can be further enhanced.

Discussion

The goal of this study was to develop a robust microscopy-based assay for interrogating AQP4 functionality in human astrocyte(-like) cells by measuring single-cell osmotic kinetics and corresponding molecular markup. To achieve this, we exploited the self-quenching property of fluorescent dyes as previously applied to measure volume changes in adherent cells[14,35]. As model system we opted for the 1321N1 astrocytoma cell line, which shows negligible endogenous *AQP4* expression and thus offers a clean platform for assessment of the role of individual isoforms and different expression levels[51,52]. Whereas the 1321N1 line has previously been used in volumetric measurements showing that these cells respond to osmotic stimuli, they have not yet been used as a platform for the stable transfection of either the M1 and M23 isoforms of AQP4 or the stable combination of both thus far[53–55]. Using the genetically modified M1M23 line that stably co-expresses both major isoforms, we compared different dosages of osmotic stimuli and established a reproducible protocol to measure osmotic cell responses in a non-lethal and reversible manner. We show that visual assessment of the cells during the experiment is important to support confident single cell segmentations and to observe undesired phenomena such as cell blebbing and cell death as they happen. The collected images also provide opportunities to discover new biological insights at the microscope or during image analysis, as for example the analysis of subregions within cells[55]. The limit to the maximum intensity change of about 30% between baseline and hyper-osmotic pulse is likely due to the adherent nature of the cells and incomplete self-quenching as also observed for confluent RPE cells[56]. Other changes to the imaging setup (*e.g.,* detector sensitivity) or the experimental setup (*e.g.,* other self-quenching dyes or loading levels) could further influence the dynamic range[57]. Quantitative metrics that represent the membrane conductivity for water flow (*e.g.,* decay rate, dynamic range…) revealed the relevance of focusing on the cellular regions, as opposed to the full field of view, as done in plate reader setups[14]. Cellular measurements were more robust to variations in cell density, which is

501 expected to occur in case of drug treatments as well and illustrated that fully confluent cultures
502 have a lower dynamic range, possibly due to the sheer crowding effect, transmembrane
503 crosslinking or as a consequence of other cell-cell interactions[58–62]. Background corrections
504 could to some extent blunt the differences between image and cell-based quantification and
505 further enhance the dynamic range but given the non-fluorogenic nature of the Calcein-AM
506 dye outside cells, the impact on a plate reader format, will be limited.
507 Single-cell analysis revealed distinct AQP4-driven kinetics, including a faster decay and
508 recovery, as well as a distinct overshoot upon return to equilibrium. This likely reflects the
509 compensatory mechanism, known as regulatory volume decrease (RVD), which has been
510 described in similar models interrogating AQP4 kinetics[63,64]. The rate at which cell swell after
511 hypo-osmotic stimuli is also thought to affect the occurrence of RVD, which could potentially
512 explain the difference we observed between WT and M1M23 after H_2O administration[64]. Even
513 within the monoclonal M1M23 cell line, we found significant variability in osmoregulation,
514 indicating that sheer AQP4 abundance is not the only modulator of the osmotic response. This
515 may in part be a consequence of the inability to distinguish cytoplasmic stores of AQP4 from
516 membrane-presented functional water channels. While we have shown the potential of NMO
517 antibodies to reveal this specific pool, targeted cell-surface biotinylation for bulk population
518 measurement (ref) or more resolved imaging techniques such as total internal reflection
519 microscopy for single cell measurement can provide a more robust, quantitative insight[17,64–67].
520 The osmotic response may also be tuned by the ratio of isoforms as has been reported
521 previously both *in vitro* as *in vivo*[5,18,68]. As we observed no differences in the osmotic response
522 rates between cells with vastly different expression levels of the individual *AQP4-M1* and
523 *AQP4-M23* isoforms, we suspected protein turnover and/or differences in membrane
524 presentation to play a role, confirming previously reported findings on isoform-specific
525 differences in OAP formation. However, further confirmation using methodologies such as cell
526 surface biotinylation would be needed[5,18,44,45,50]. Human primary astrocytes (SC1800) did not

show an enhanced osmoregulation as compared to WT astrocytoma cells either, which may be due to their fetal nature and their proliferative state. A lack of the appropriate environmental cues and/or timing precludes these cells from achieving the mature phenotype that is required for adequate *AQP4* expression and membrane presentation[25,69]. The same possibly holds true for the iPSC-derived astrocytes (APC and iSOX). Although an increase of *AQP4* expression has been documented for the iSOX line on day 30 compared to day 5 of maturation, the expression level was still much lower than that of SC1800[34]. Conversely, given the limited enhancement of osmoregulation observed in the latter, it seems plausible that the constitutive overexpression of *AQP4* in the M1M23 cells leads to an exaggerated response. However, a more extensive comparison between these different cells is warranted to better understand which physiological levels of AQP4 are required for enhanced osmoregulation and what cell-intrinsic and -extrinsic factors contribute to its functionality. WT and M1M23 cells alongside more physiologically relevant models could also be used as positive and negative controls for the osmotic responses and provide controls to correct for batch effects in larger experimental settings.

One crucial external factor is the extracellular matrix, as it is known to affect the turnover and membrane presentation of AQP4[49,50]. Recognizing the limitations of working with confocal projections (and possible improvements such as TIRF mentioned above), we confirmed an increased colocalization of AQP4 with membrane-presented CD44 when cells were cultured onto PLO and laminin coated substrates, suggestive of increased AQP4 membrane enrichment without changes in expression levels, as previously reported in primary rat cultures[70,71]. Building on this, we enforced a polarized phenotype using micropatterns, and documented an accelerated response to osmotic stimuli. It should be noted that given the fast-growing character of 1321N1 cells, modifications to the growth conditions will be needed to increase the experimental timeframe beyond the current 4 hours.

To conclude, we have optimized a robust microscopy assay that measures the osmoregulation in individual human astrocytoma cells and have correlated this live-cell readout with post-hoc quantification of their total AQP4 levels. Through chemical and spatial substrate modifications, we have shown it is possible to increase AQP4 membrane enrichment in these cells as well as their osmotic response. Using the same methodology we found a limited evidence for AQP4-driven osmoregulation in primary or iPSC-derived human astrocytes, suggesting they are in an immature state. While currently we only used indirect means to distinguish membrane-presented from total cellular AQP4, the showed the potential of NMO antibodies to further refine the assay. Yet, given its flexibility and scalability, our current approach can be used to screen for regulators of AQP4 functionality with high fidelity and single-cell resolution.

Author contributions

HS, PL, WDV and RN were responsible for conceptualization. HS, SDB, WDV, RN, PP, NHEL and VS were responsible for methodology. HS, SDB and WDV were responsible for the development of software. Experiments were coordinated by HS and EVB and performed by HS and SDB. Formal analyses and visualizations were performed by HS and WDV. Supervision was provided by WDV, HM and RN. Original draft and revision by HS and WDV, with review and editing by all co-authors. All authors revised and approved the final version of this manuscript.

Funding

This work was funded by Fonds Wetenschappelijk Onderzoek Vlaanderen (1SB7423N; I000123N; I003420N) and IOF UAntwerpen (FFI210239; FFI230099) and VLAIO (HBC.2018.0207).

Acknowledgements

We thank Dr. Stefan Masure (Janssen Pharmaceutica, Belgium) for providing the 4 astrocytoma cell lines, Roel De Jongh and Margot Dombrecht for their technical assistance with the quenching assay and Marlies Verschuuren for advising on data analysis.

Data availability statement

The authors report that the results of this study are available within the manuscript and supplementary materials. All image analysis scripts are open-source available on GitHub (https://github.com/DeVosLab)

Conflict of interest

The authors declare no conflict of interest.

590 **References**

591 1. Neely, J. D., Christensen, B. M., Nielsen, S. & Agre, P. Heterotetrameric Composition
592 of Aquaporin-4 Water Channels. *Biochemistry* **38**, 11156–11163 (1999).
593 2. Smith, A. J. & Verkman, A. S. Superresolution Imaging of Aquaporin-4 Cluster Size in
594 Antibody-Stained Paraffin Brain Sections. *Biophys. J.* **109**, 2511–2522 (2015).
595 3. de Bellis, M. *et al.* Orthogonal arrays of particle assembly are essential for normal
596 aquaporin-4 expression level in the brain. *Glia* **69**, 473–488 (2021).
597 4. Jorgačevski, J., Zorec, R. & Potokar, M. Insights into Cell Surface Expression,
598 Supramolecular Organization, and Functions of Aquaporin 4 Isoforms in Astrocytes.
599 *Cells* vol. 9 2622 (2020).
600 5. Smith, A. J., Jin, B. J., Ratelade, J. & Verkman, A. S. Aggregation state determines the
601 localization and function of M1- and M23-aquaporin-4 in astrocytes. *J. Cell Biol.* **204**,
602 559–573 (2014).
603 6. Rasmussen, M. K., Mestre, H. & Nedergaard, M. The glymphatic pathway in
604 neurological disorders. *The Lancet Neurology* vol. 17 (2018).
605 7. Verkman, A. S., Phuan, P.-W., Asavapanumas, N. & Tradtrantip, L. Biology of AQP4
606 and Anti-AQP4 Antibody: Therapeutic Implications for NMO STRUCTURE AND
607 WATER TRANSPORT FUNCTION OF AQUAPORIN-4 (AQP4). (2013)
608 doi:10.1111/bpa.12085.
609 8. Zeppenfeld, D. M. *et al.* Association of perivascular localization of aquaporin-4 with
610 cognition and Alzheimer disease in aging brains. *JAMA Neurol.* **74**, 91–99 (2017).
611 9. Yang, J. *et al.* Loss of astrocyte polarization in the Tg-ArcSwe mouse model of
612 Alzheimer's disease. *J. Alzheimer's Dis.* **27**, 711–722 (2011).
613 10. Ahnaou, A. & Drinkenburg, W. H. I. . Sleep, neuronal hyperexcitability, inflammation
614 and neurodegeneration: does early chronic short sleep trigger and is it the key to
615 overcoming Alzheimer's disease? *Neurosci. Biobehav. Rev.* (2021)

doi:10.1016/J.NEUBIOREV.2021.06.039.

11. Ooms, S. *et al.* Effect of 1 night of total sleep deprivation on cerebrospinal fluid ??-amyloid 42 in healthy middle-aged men a randomized clinical trial. *JAMA Neurol.* **71**, 971–977 (2014).

12. Vlassenko, A. G. *et al.* Imaging and cerebrospinal fluid biomarkers in early preclinical Alzheimer disease HHS Public Access Author manuscript. *Ann Neurol* **80**, 379–387 (2016).

13. Silva, I., Silva, J., Ferreira, R. & Trigo, D. Glymphatic system, AQP4, and their implications in Alzheimer's disease. *Neurol. Res. Pract.* **3**, 5 (2021).

14. Mola, M. G., Nicchia, G. P., Svelto, M., Spray, D. C. & Frigeri, A. Automated cell-based assay for screening of aquaporin inhibitors. *Anal. Chem.* **81**, 8219–8229 (2009).

15. Chi, Y., Gao, K., Zhang, H., Takeda, M. & Yao, J. Suppression of cell membrane permeability by suramin: involvement of its inhibitory actions on connexin 43 hemichannels. *Br. J. Pharmacol.* **171**, 3448 (2014).

16. Kitchen, P. *et al.* Targeting Aquaporin-4 Subcellular Localization to Treat Central Nervous System Edema. *Cell* **181**, 784-799.e19 (2020).

17. Crane, J. M. & Verkman, A. S. Reversible, temperature-dependent supramolecular assembly of aquaporin-4 orthogonal arrays in live cell membranes. *Biophys. J.* **97**, 3010–3018 (2009).

18. Pisani, F. *et al.* Regulation of aquaporin-4 expression in the central nervous system investigated using M23-AQP4 null mouse. *Glia* **69**, 2235–2251 (2021).

19. De Bellis, M. *et al.* A novel human aquaporin-4 splice variant exhibits a dominant-negative activity: a new mechanism to regulate water permeability. *Mol. Biol. Cell* **25**, 470–80 (2014).

20. Solenov, E., Watanabe, H., Manley, G. T. & Verkman, A. S. Sevenfold-reduced osmotic water permeability in primary astrocyte cultures from AQP-4-deficient mice, measured

by a fluorescence quenching method. *Am. J. Physiol. Physiol.* **286**, C426–C432 (2004).

21. Huber, V. J., Tsujita, M. & Nakada, T. Identification of Aquaporin 4 inhibitors using in vitro and in silico methods. *Bioorg. Med. Chem.* **17**, 411–417 (2009).

22. Moe, S. E. *et al.* New isoforms of rat Aquaporin-4. *Genomics* **91**, 367–377 (2008).

23. De Bellis, M. *et al.* Translational readthrough generates new astrocyte AQP4 isoforms that modulate supramolecular clustering, glial endfeet localization, and water transport. *Glia* **65**, 790–803 (2017).

24. Eidsvaag, V. A., Enger, R., Hansson, H. A., Eide, P. K. & Nagelhus, E. A. Human and mouse cortical astrocytes differ in aquaporin-4 polarization toward microvessels. *Glia* **65**, 964–973 (2017).

25. Zhang, Y. *et al.* Purification and Characterization of Progenitor and Mature Human Astrocytes Reveals Transcriptional and Functional Differences with Mouse. *Neuron* **89**, 37–53 (2016).

26. Tarassishin, L., Suh, H. S. & Lee, S. C. LPS and IL-1 differentially activate mouse and human astrocytes: Role of CD14. *Glia* **62**, 999–1013 (2014).

27. Arciénega, I. I., Brunet, J. F., Bloch, J. & Badaut, J. Cell locations for AQP1, AQP4 and 9 in the non-human primate brain. *Neuroscience* **167**, 1103–1114 (2010).

28. Toft-Bertelsen, T. L. *et al.* Clearance of activity-evoked K + transients and associated glia cell swelling occur independently of AQP4 : A study with an isoform-selective AQP4 inhibitor. *Glia* glia.23851 (2020) doi:10.1002/glia.23851.

29. Debaker, C. *et al.* Diffusion MRI reveals in vivo and non-invasively changes in astrocyte function induced by an aquaporin-4 inhibitor. *PLoS One* **15**, (2020).

30. Alghanimy, A., Martin, C., Gallagher, L. & Holmes, W. M. The effect of a novel AQP4 facilitator, TGN-073, on glymphatic transport captured by diffusion MRI and DCE-MRI. *PLoS One* **18**, e0282955 (2023).

31. Huber, V. J., Igarashi, H., Ueki, S., Kwee, I. L. & Nakada, T. Aquaporin-4 facilitator

668 TGN-073 promotes interstitial fluid circulation within the blood-brain barrier: [17 O]H
669 2 O JJVCPE MRI study. *Neuroreport* **29**, 697–703 (2018).
670 32. Boeren, M. *et al.* Activation of Interferon-Stimulated Genes following Varicella-Zoster
671 Virus Infection in a Human iPSC-Derived Neuronal In Vitro Model Depends on
672 Exogenous Interferon-α. *Viruses* **14**, 2517 (2022).
673 33. TCW, J. *et al.* An Efficient Platform for Astrocyte Differentiation from Human Induced
674 Pluripotent Stem Cells. *Stem Cell Reports* **9**, 600–614 (2017).
675 34. Neyrinck, K. *et al.* SOX9-induced Generation of Functional Astrocytes Supporting
676 Neuronal Maturation in an All-human System. *Stem Cell Rev. Reports* **17**, 1855–1873
677 (2021).
678 35. Hamann, S. *et al.* Measurement of Cell Volume Changes by Fluorescence Self-
679 Quenching. *J. Fluoresc.* **12**, 139–145 (2002).
680 36. Schindelin, J. *et al.* Fiji: An open-source platform for biological-image analysis. *Nat.*
681 *Methods* **9**, 676–682 (2012).
682 37. R Core Team (2021) R: A Language and Environment for Statistical Computing. R
683 Foundation for Statistical Computing, Vienna. https://www.r-project.org (2021).
684 38. Christopoulos, D. T. On the Efficient Identification of an Inflection Point On the
685 Efficient Identification of an Inflection Point. *Int. J. Math. Sci. Comput.* **6**, 13–20 (2016).
686 39. Stringer, C., Wang, T., Michaelos, M. & Pachitariu, M. Cellpose: a generalist algorithm
687 for cellular segmentation. *Nat. Methods* **18**, 100–106 (2021).
688 40. De Vos, W. H., Van Neste, L., Dieriks, B., Joss, G. H. & Van Oostveldt, P. High content
689 image cytometry in the context of subnuclear organization. *Cytom. Part A* **77**, 64–75
690 (2010).
691 41. Schmidt, U., Weigert, M., Broaddus, C. & Myers, G. Cell detection with star-convex
692 polygons. *Lect. Notes Comput. Sci. (including Subser. Lect. Notes Artif. Intell. Lect.*
693 *Notes Bioinformatics)* **11071 LNCS**, 265–273 (2018).

42. Bolte, S. & Cordelières, F. P. A guided tour into subcellular colocalization analysis in light microscopy. *J. Microsc.* **224**, 213–232 (2006).

43. Posit Team. RStudio: Integrated Development Environment for R. (2023).

44. Nagelhus, E. A. & Ottersen, O. P. Physiological Roles of Aquaporin-4 in Brain. *Physiol. Rev.* **93**, 1543–1562 (2013).

45. Crane, J. M., Bennett, J. L. & Verkman, A. S. Live cell analysis of aquaporin-4 M1/M23 interactions and regulated orthogonal array assembly in glial cells. *J. Biol. Chem.* **284**, 35850–35860 (2009).

46. Huang, M., Camara, A. K. S., Stowe, D. F., Qi, F. & Beard, D. A. Mitochondrial Inner Membrane Electrophysiology Assessed by Rhodamine-123 Transport and Fluorescence. *Ann. Biomed. Eng.* **35**, 1276 (2007).

47. Fam, K. T. *et al.* Rational Design of Self-Quenched Rhodamine Dimers as Fluorogenic Aptamer Probes for Live-Cell RNA Imaging. *Anal. Chem.* **94**, 6657–6664 (2022).

48. TCW, J. *et al.* An Efficient Platform for Astrocyte Differentiation from Human Induced Pluripotent Stem Cells. *Stem Cell Reports* **9**, 600–614 (2017).

49. Noël, G., Stevenson, S. & Moukhles, H. A high throughput screen identifies chemical modulators of the laminin-induced clustering of dystroglycan and aquaporin-4 in primary astrocytes. *PLoS One* **6**, e17559 (2011).

50. Tham, D. K. L., Joshi, B. & Moukhles, H. Aquaporin-4 cell-surface expression and turnover are regulated by dystroglycan, dynamin, and the extracellular matrix in astrocytes. *PLoS One* **11**, e0165439 (2016).

51. Mostafavi, H. *et al.* Fluoxetin Upregulates Connexin 43 Expression in Astrocyte. *Basic Clin. Neurosci.* **5**, 74 (2014).

52. Amro, Z., Collins-Praino, L. E. & Yool, A. J. Protective roles of peroxiporins AQP0 and AQP11 in human astrocyte and neuronal cell lines in response to oxidative and inflammatory stressors. *Biosci. Rep.* **44**, 20231725 (2024).

720 53. Blum, A. E., Walsh, B. C. & Dubyak, G. R. Extracellular osmolarity modulates G
721 protein-coupled receptor-dependent ATP release from 1321N1 astrocytoma cells. *Am.*
722 *J. Physiol. - Cell Physiol.* **298**, 386–396 (2010).
723 54. Saito, M., Tanaka, H., Sasaki, M., Kurose, H. & Nakahata, N. Involvement of aquaporin
724 in thromboxane A2 receptor-mediated, G12/13/RhoA/NHE-sensitive cell swelling in
725 1321N1 human astrocytoma cells. *Cell. Signal.* **22**, 41–46 (2010).
726 55. Žugec, M. *et al.* Plectin plays a role in the migration and volume regulation of astrocytes:
727 a potential biomarker of glioblastoma. *J. Biomed. Sci.* **31**, 1–22 (2024).
728 56. Hamann, S. *et al.* Measurement of Cell Volume Changes by Fluorescence. **12**, (2002).
729 57. Solenov, E., Watanabe, H., Manley, G. T. & Verkman, A. S. Sevenfold-reduced osmotic
730 water permeability in primary astrocyte cultures from AQP-4-deficient mice, measured
731 by a fluorescence quenching method. *Am J Physiol Cell Physiol* **286**, 426–432 (2004).
732 58. Li, J. *et al.* Astrocyte-to-astrocyte contact and a positive feedback loop of growth factor
733 signaling regulate astrocyte maturation. *Glia* **67**, 1571–1597 (2019).
734 59. Tham, D. K. L., Joshi, B. & Moukhles, H. Aquaporin-4 cell-surface expression and
735 turnover are regulated by dystroglycan, dynamin, and the extracellular matrix in
736 astrocytes. *PLoS One* **11**, e0165439 (2016).
737 60. Thompson, O. *et al.* Modulation of cell spreading and cell-substrate adhesion dynamics
738 by dystroglycan. *J. Cell Sci.* **123**, 118–127 (2010).
739 61. Potokar, M., Morita, M., Wiche, G. & Jorgačevski, J. The Diversity of Intermediate
740 Filaments in Astrocytes. *Cells* **9**, (2020).
741 62. Geiger, B., Bershadsky, A., Pankov, R. & Yamada, K. M. Transmembrane extracellular
742 matrix-cytoskeleton crosstalk. *Nat. Rev. Mol. Cell Biol.* **2**, 793–805 (2001).
743 63. Benfenati, V. *et al.* An aquaporin-4/transient receptor potential vanilloid 4
744 (AQP4/TRPV4) complex is essential for cell-volume control in astrocytes. *Proc. Natl.*
745 *Acad. Sci. U. S. A.* **108**, 2563–2568 (2011).

64. Mola, M. G. *et al.* The speed of swelling kinetics modulates cell volume regulation and calcium signaling in astrocytes: A different point of view on the role of aquaporins. *Glia* **64**, 139–154 (2016).

65. Rao, K. V. R. *et al.* Aquaporin-4 in manganese-treated cultured astrocytes. *Glia* **58**, 1490–1499 (2010).

66. Tham, D. K. L., Joshi, B. & Moukhles, H. Aquaporin-4 cell-surface expression and turnover are regulated by dystroglycan, dynamin, and the extracellular matrix in astrocytes. *PLoS One* **11**, e0165439 (2016).

67. Bae, W., Yoon, T. Y. & Jeong, C. Direct evaluation of self-quenching behavior of fluorophores at high concentrations using an evanescent field. *PLoS One* **16**, (2021).

68. Smith, A. J. & Verkman, A. S. Superresolution Imaging of Aquaporin-4 Cluster Size in Antibody-Stained Paraffin Brain Sections. *Biophys. J.* **109**, 2511–2522 (2015).

69. Sloan, S. A. *et al.* Human Astrocyte Maturation Captured in 3D Cerebral Cortical Spheroids Derived from Pluripotent Stem Cells. *Neuron* **95**, 779-790.e6 (2017).

70. Noël, G., Tham, D. K. L., MacVicar, B. A. & Moukhles, H. Agrin plays a major role in the coalescence of the aquaporin-4 clusters induced by gamma-1-containing laminin. *J. Comp. Neurol.* **528**, 407–418 (2020).

71. Dzwonek, J. & Wilczynski, G. M. CD44: molecular interactions, signaling and functions in the nervous system. *Front. Cell. Neurosci.* **9**, 175 (2015).

Figures

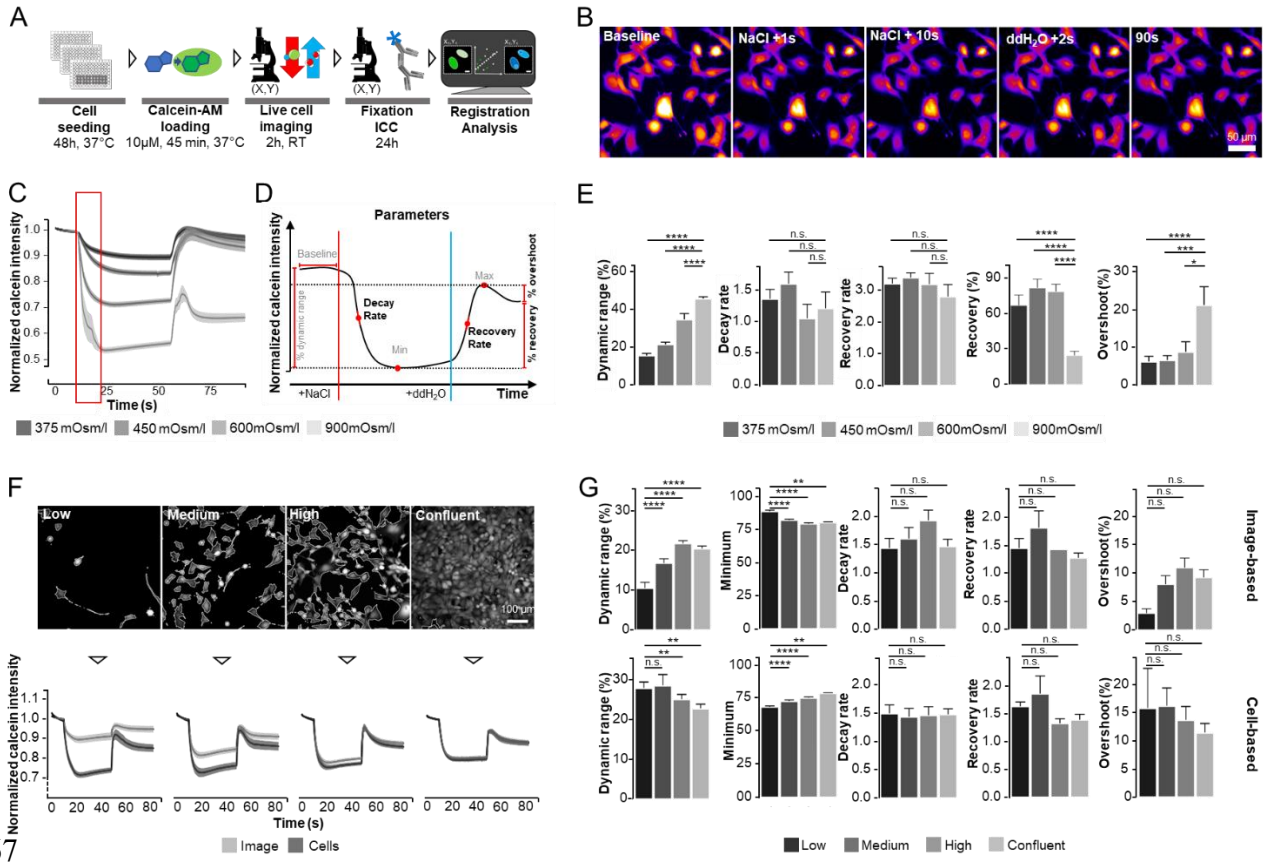

Figure 1. Validation of live cell imaging osmotic assay. A. Schematic representation of the live-cell assay. B. Visual overview of key moments during live cell imaging. Cellular fluorescence decreased after NaCl administration, stabilized and increased again after ddH_2O administration. At the end of the sequence fluorescence was lower than at baseline, even after correcting for photobleaching indicating incomplete signal recovery. C. Dose-response curve of M1M23 cells stimulated with hyperosmotic NaCl at 10s and the H_2O injection at 60s to return to isotonicity. E. Schematic representation of the parameters that are extracted from the fluorescence time curve. The red line indicates the moment of hyperosmotic solution administration. The blue line indicates the moment of H_2O administration to return to isotonicity. E. Parameter quantification of M1M23 cells stimulated with the NaCl dose series. F. Sample images of M1M23 cells loaded with calcein-AM at different cell densities. Below each image the corresponding mean normalized calcein intensity and standard error are

displayed, showing the effect of cell-density on dynamic range for image- versus cell-based intensity quantification in cells stimulated with 600mOsm/l NaCl solution. G. Image- versus cell-based parameter quantification showed an overall larger dynamic range and more stable baseline signal when isolating cells from images when cell density was varied. This also impacted the minimum intensity of the curve. Cell density had no significant effect on decay rate, recovery rate or overshoot. One-way ANOVA (Dunnett with 900mOsm/l as control; E) / (Dunnett with low density as control; G): * $p < 0.05$, ** <0.01, *** <0.001, **** <0.0001. All values except baseline (intensity), decay rate and recovery rate are percentages, scaled to the highest value. Error bars and ribbons represent well-level standard error. Threshold-based segmentation was performed, with (C, E) and without watershed separation (F, G).

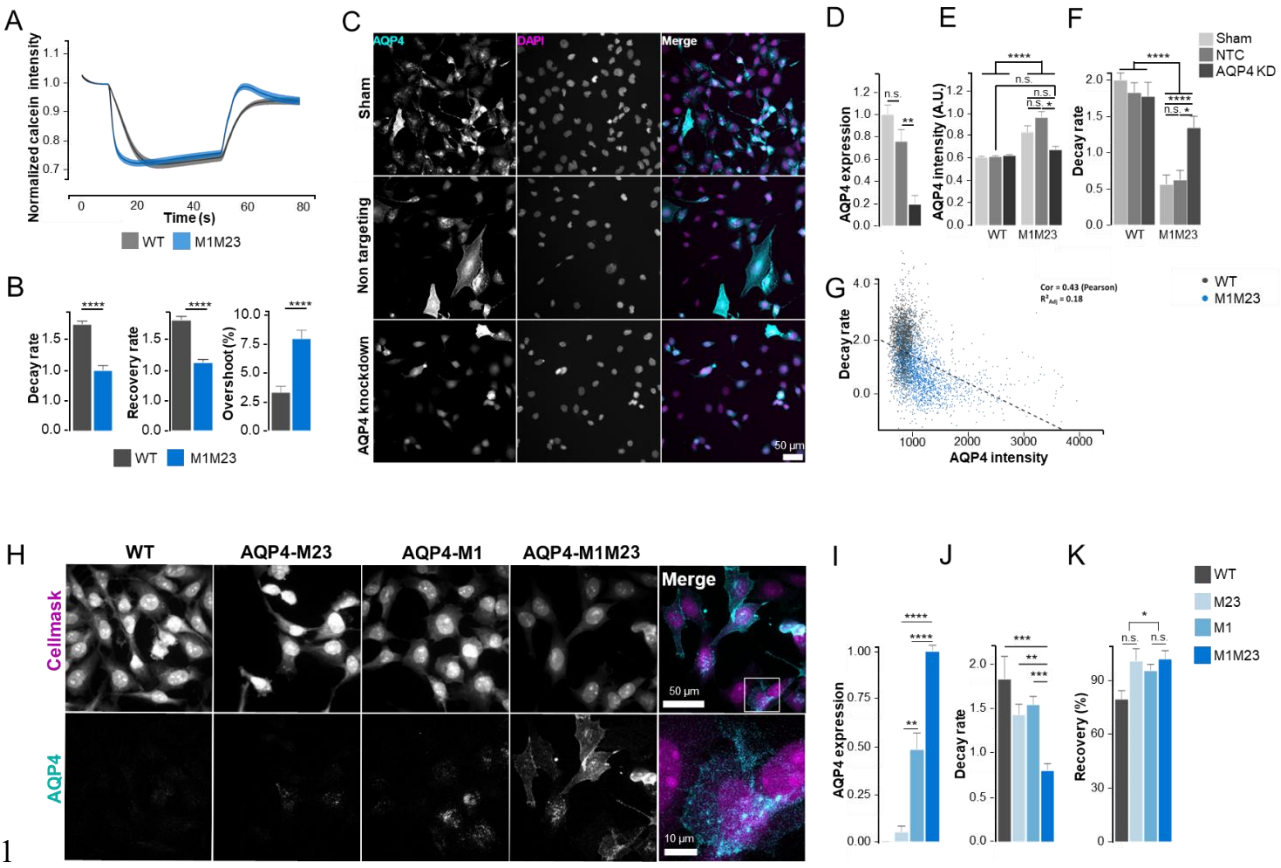

Figure 2. 1321N1 astrocytoma cells overexpressing human AQP4 showed a significant difference in response to both hyperosmotic and hypoosmotic stimuli. A. Co-expression of

AQP4-M1 and *AQP4-M23* increased the rate at which 1321N1 cells respond to changes in osmotic pressure in the micro-environment. B. M1M23 cells showed a stronger response after stimulation and a faster attenuation with a detectable overshoot after returning to isotonicity. Overshoot and recovery are expressed as percentages. C. Sample images showing the siRNA-mediated knockdown of *AQP4* decreased overall AQP4 protein abundance in M1M23 cells. D. Using RT-qPCR, the knockdown of *AQP4* was validated at 48 hours after transduction. E. Image analysis confirmed a reduction in total AQP4 protein at 72 hours after transduction. F. siRNA-mediated knockdown of *AQP4* in had a strong impact on the rate at which cells responded to changes in osmotic pressure. G. On the single-cell level, there was moderate correlation between AQP4 intensity and decay rate (Pearson correlation = 0.43, $R^2 = 0.18$). H. Immunofluorescent images highlight differences between the presentation of the human AQP4 isoforms. AQP4 was visible in a punctate or diffuse manner. I. RT-qPCR showed that the M1M23 line has a proportionally higher expression of total *AQP4* mRNA. J. The combined presence of AQP4-M1 and AQP4-M23 amplified the rate at which cells respond to changes in osmotic pressure. K. M23 and M1M23 cells showed a higher recovery than WT. Unpaired t-test (B); One-way ANOVA (Dunnett with M1M23 as control; D, J)/ (Tukey; E, F, I, K). * $p < 0.05$, ** <0.01, *** <0.001, **** <0.0001. Error bars and ribbons represent well-level standard error.

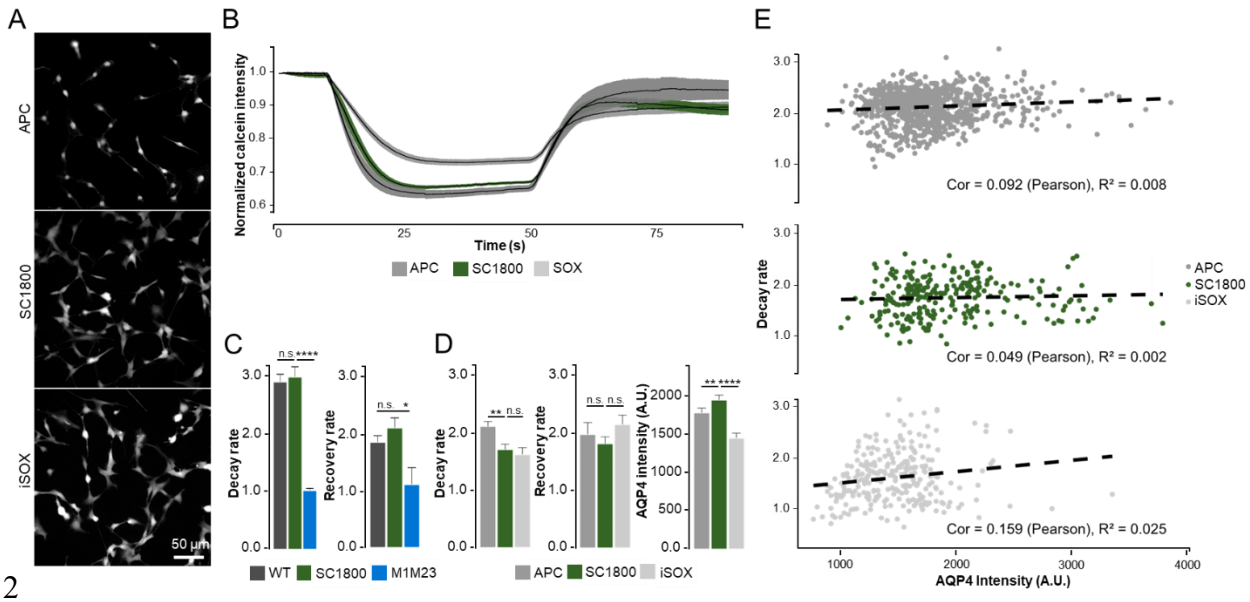

Figure 3. Human primary and iPSC-derived astrocytes show much less pronounced osmotic responses upon hyperosmotic and hypoosmotic stimulations. A. Calcein-AM images showing the fetal phenotype with a branching and clustering morphology of the used human iPSC-derived and primary astrocytes. B. Mean intensity traces of the APC, iSOX and SC1800 cells, with the iSOX astrocytes showing a higher minimum compared to the other two lines. C. Decay and recovery rate of SC1800 after 10 passages, compared to the WT and M1M23 cell lines. The SC1800 do not differ from WT in both responses. D. Separate comparison of APC, iSOX and SC1800 decay and recovery rates, besides the AQP4 intensity measured in these cells (continuation of B). E. Single-cell correlation plots of APC, iSOX and SC1800 cells showing very limited correlation with total AQP4. One-way ANOVA (Dunnett with SC1800 as control; C, D) $p < 0.05$, ** <0.01, *** <0.001, **** <0.0001. Error bars and ribbons represent well-level standard error. APC: SC1801-induced astrocyte precursor cells, SC1800: primary astrocytes, iSOX: SOX9-induced astrocyte precursor cells

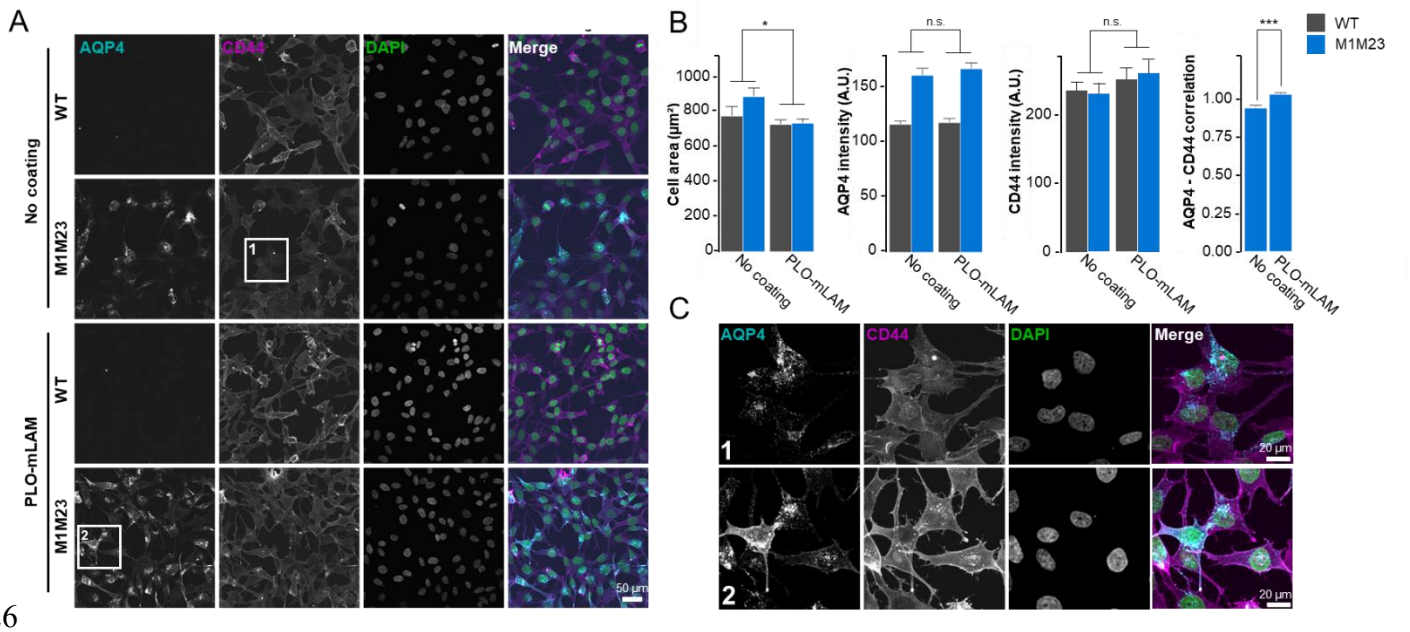

826

827 **Figure 4.** Seeding astrocytoma on PLO-mLAM coated plates modifies cell size and AQP4
828 presentation. A. Comparison of WT and M1M23 cells on regular plastic bottom plates and
829 plastic bottom plates coated with PLO-mLAM . B. The presence of laminin reduces cell growth
830 area and improves the correlation between cell membrane receptor CD44 and AQP4 without
831 increasing protein abundance for either protein. C. M1M23 cells on PLO-mLAM coated plates
832 appear to have an increased CD44 presentation at the cell membrane, as well as a substantial
833 increase of AQP4 at the cell membrane. Brightness and contrast are adapted compared to A.
834 Two-way ANOVA (Tukey; B first 3 panels); unpaired t-test (B right panel). * $p < 0.05$, **
835 <0.01, *** <0.001, **** <0.0001. Error bars and ribbons represent well-level standard error.
836 PLO: poly-L-ornithine, mLAM: mouse laminin NMO: *neuromyelitis Optica*, NPC: no-primary
837 control, PS: patient serum, HS: healthy control serum.

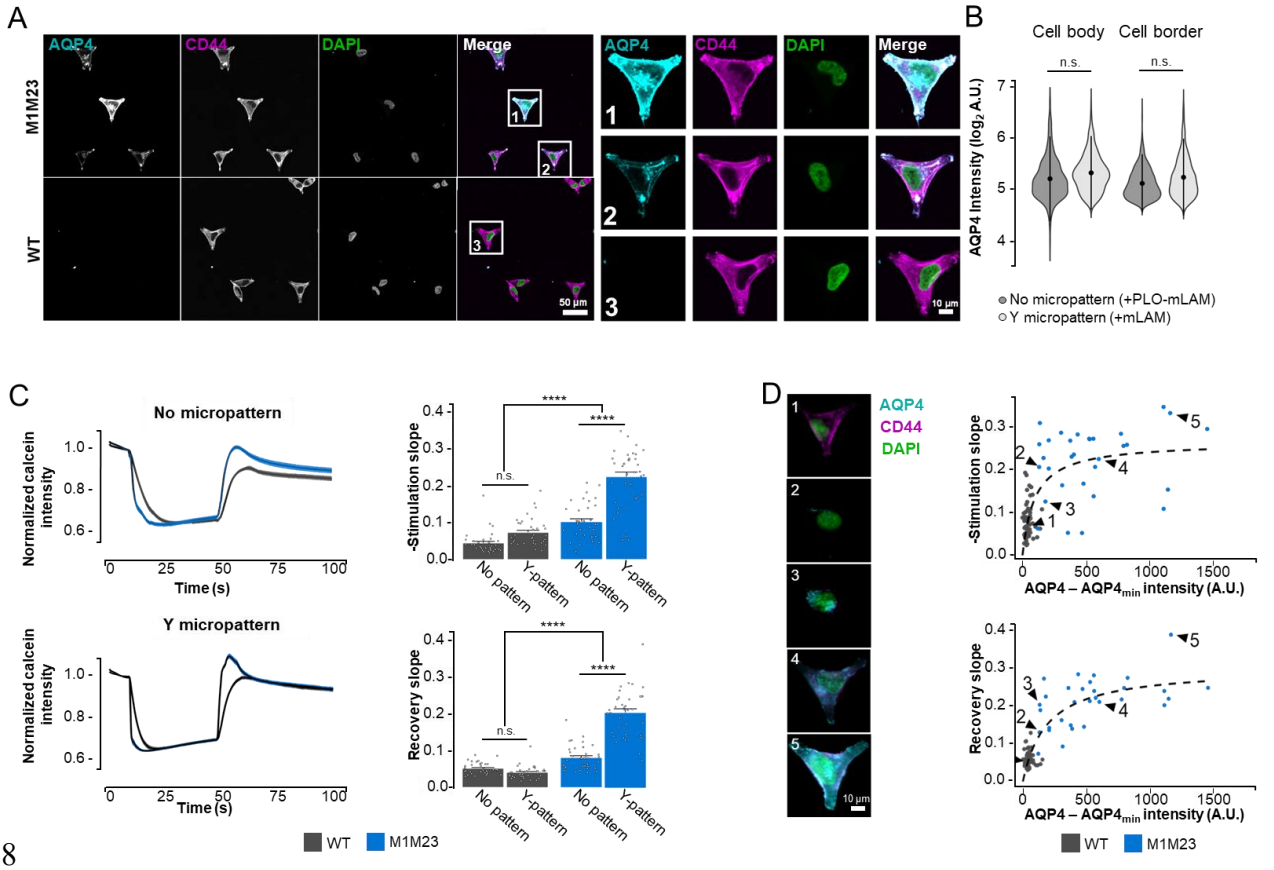

838

839

840 **Figure 5.** Astrocytoma spread out on micropatterned plates show indications of changes in
841 AQP4 presentation and functionality. A. Images showing that while the variability in AQP4
842 abundance and presentation is still present in the M1M23 cell line, cells with a very high AQP4
843 abundance at the membrane can be observed. B. When dividing the cell in a cytoplasmic and
844 a border ROI, comprising of a 5 pixel boundary region, no significant change in mean AQP4
845 intensity is observed, yet the data suggests a reduced variability in the cell body region. C. Cells
846 on Y-micropatterns show a much faster mean decay rate and recovery rate than cells on regular
847 plates with PLO-mLAM coating, as well as larger differences between WT and M1M23. D.
848 Overview of slow and fast responding cell on Y-micropatterns. With increasing AQP4
849 abundance, the response to osmotic stimuli increases. After a certain level however, the effect
850 is reduced. The relationship between the osmotic response slope and shifted AQP4 intensity
851 (AQP4 – $AQP4_{min}$) can be modeled with the Michaelis-Menten model for enzyme kinetics (p

852 = $1.999.10^{-5}$ for -stimulation slope with residual SE = 0.061, $p < 8.85.10^{-8}$ for recovery slope
853 with residual SE = 0.042). All error bars and ribbons represent cell-level standard error, dots
854 represent 35 individual cells in 2-3 wells per condition, imaged on a single day. One-way
855 ANOVA with Tukey post-hoc test (B, C). ROI: region-of-interest, PLO: poly-L-ornithine,
856 mLAM: mouse laminin.